Journal of Materials Chemistry A

ROYAL SOCIETY OF CHEMISTRY

PAPER

View Article Online
View Journal



Cite this: DOI: 10.1039/d4ta02438a

# Solution-processable $Ni_3(HITP)_2$/MXene heterostructures for ppb-level gas detection†

Xuanhao Wu,‡[a] Mengmeng Niu,‡[b] Xin Tian,[c] Xiaoyan Peng,[a] Pio John S. Buenconsej,[d] Xu Wu,[b] Yeliang Wang,[b] Wei Ji,[e] Yi Li,[f] Jingsi Qiao,*[b] Jifang Tao,[c] Mingming Zhang,[a] Song Xiao*[f] and Hongye Yuan *[a]

Developing sensitive metal–organic framework (MOF) systems to overcome the ubiquitous trade-off between porosity and conductivity remains a formidable yet sought-after endeavor. This pursuit is of great significance for the development of MOF-based chemiresistive sensors with enhanced sensitivity and selectivity. Herein, we present an innovative template assisted strategy that utilizes the two-dimensional properties and good conductivity of MXene nanosheets, as well as lattice matching between MXene ($Nb_2C$) and selected $Ni_3(HITP)_2$, to achieve controllable self-assembly of $Ni_3(HITP)_2$ on MXene sheets. This results in $Ni_3(HITP)_2$/MXene (HITP: 2,3,6,7,10,11-hexaaminotriphenylene) heterostructures with considerable conductivity, porosity, and solution processability. The powder and film electrical conductivity are $4.8 \times 10^3$ and $5.3 \times 10^5$ S m$^{-1}$, respectively, and the BET specific surface area can reach 797.8 m$^2$ g$^{-1}$. It is worth noting that excellent solution processability helps to prepare large-area films (23 cm × 9 cm) with good uniformity. Gas sensors based on $Ni_3(HITP)_2$/MXene heterostructures exhibit high sensitivity (LOD ~ 5 ppb) and selectivity towards ultratrace ethanol at room temperature, setting a new benchmark. Such sensing behavior stems from the strong coupling of $Ni_3(HITP)_2$/MXene heterostructures and their enhanced interaction with ethanol, evidenced by experimental results and theoretical calculations. Real-time respiratory sensing assessments underscore their practicality in healthcare monitoring. This straightforward approach simplifies the integration of MOF-related materials on miniaturized devices with outstanding performance.

Received 9th April 2024
Accepted 7th June 2024

DOI: 10.1039/d4ta02438a

rsc.li/materials-a



## Introduction

The escalating concern pertaining to industrial gas leakage detection, urban planning, healthcare monitoring, modern agriculture, and food freshness assessment has recently led to a steady augmentation of the gas sensor market, projected to reach a value of US $4.002 billion by 2025.[1–3] The widespread deployment of gas sensors of high performance in constructing sensor networks for smart cities including internet of things (IoT) and industrial internet of things (IIoT) is conceptually regarded as a strategic approach to address the aforementioned anxiety.[1–5] The key lies in the design and synthesis of highly sensitive materials with considerable responsiveness in terms of electric, dielectric, magnetic, optical, thermometric, and acoustic fluctuation toward specific gaseous analytes. Metal–organic frameworks (MOFs), alternatively recognized as porous coordination polymers (PCPs), represent a novel class of porous materials constructed *via* the assembly of metal ions/clusters with organic ligands. Their designability in structural topology, porosity, host–guest interactions, and physicochemical properties[6–8] holds tremendous potential for diverse applications including gas adsorption/separation,[9] heterogeneous catalysis,[10] chemical sensing,[1–5] drug delivery,[11] *etc.* Harnessing the custom-made specific surface area, pore size/geometry, and host–guest interactions of MOFs facilitates selective enrichment of targeted gases.[12,13] This, in turn, results in substantially elevated sensitivity and selectivity for gas detection.

Significant advancements have been made so far toward the fabrication of MOF-based chemiresistive sensors with salient

[a]State Key Laboratory for Mechanical Behavior of Materials, Shaanxi International Research Center for Soft Matter, School of Materials Science and Engineering, Xi'an Jiaotong University, Xi'an, 710049, P. R. China. E-mail: hongye.yuan@xjtu.edu.cn
[b]Advanced Research Institute of Multidisciplinary Sciences, School of Integrated Circuits and Electronics, Beijing Institute of Technology, Beijing 100081, China. E-mail: qiaojs@bit.edu.cn
[c]School of Information Science and Engineering, Shandong University, Qingdao, 266237, P. R. China
[d]Facility for Analysis Characterization Testing Simulation (FACTS), Nanyang Technological University, 50 Nanyang Avenue, 639798, Singapore
[e]Beijing Key Laboratory of Optoelectronic Functional Materials & Micro-Nano Devices, Department of Physics, Renmin University of China, Beijing 100872, China
[f]State Key Laboratory of Power Grid Environmental Protection (School of Electrical Engineering and Automation), Wuhan University, Wuhan 430072, Hubei Province, China. E-mail: xiaosong@whu.edu.cn

† Electronic supplementary information (ESI) available. See DOI: https://doi.org/10.1039/d4ta02438a

‡ Contributed equally to this work.

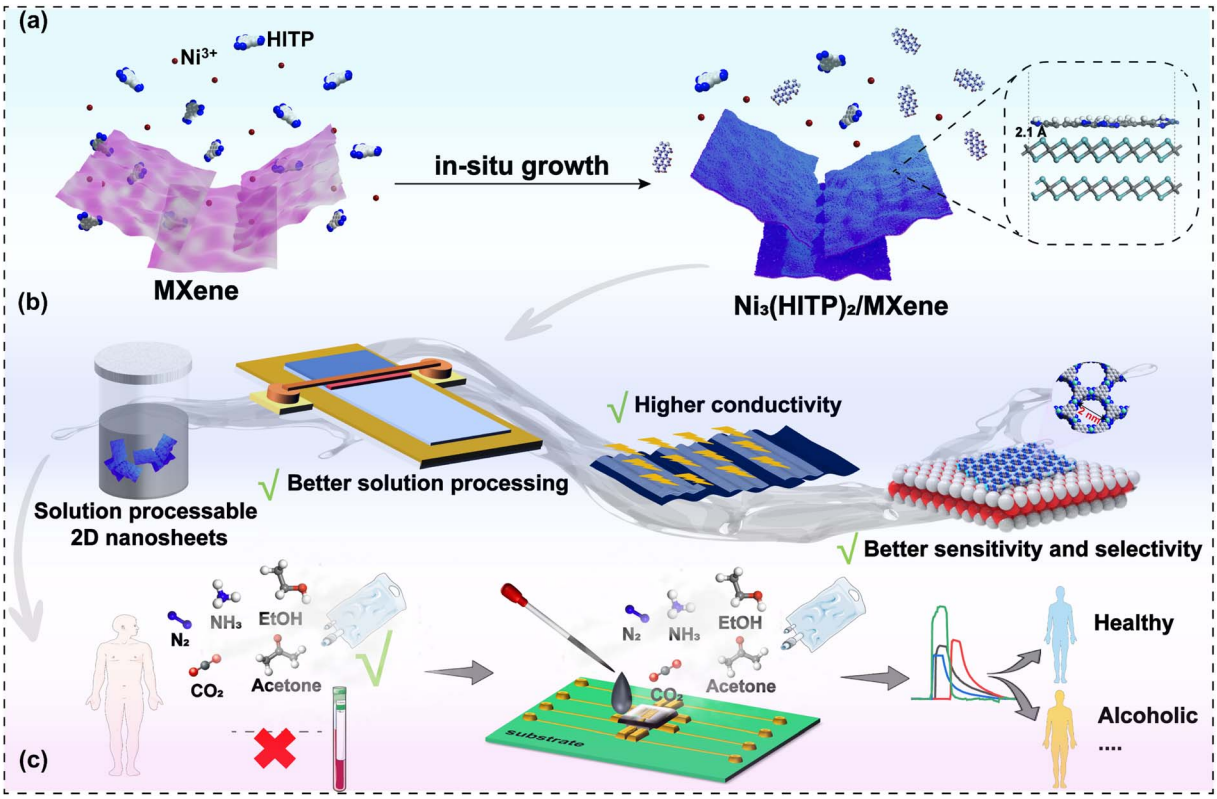


Fig. 1 Schematic diagram on the synthesis strategy of $Ni_3(HITP)_2$/MXene heterostructure and its application for sensing and detection at room temperature. (a) Schematic illustration of the direct synthesis strategy for constructing $Ni_3(HITP)_2$/MXene heterostructures. (b) Key benefits of $Ni_3(HITP)_2$/MXene heterostructures, showcasing their outstanding solution processability, remarkable electrical conductivity, and better sensitivity and selectivity toward targeted analytes. (c) Functional module of the sensors based on $Ni_3(HITP)_2$/MXene heterostructures employed in real-time gas monitoring at room temperature to assess human health status.

sensing performance towards a series of analytes.[12–21] For example, Zhang *et al.* demonstrated excellent selectivity of sensors based on ZnO@ZIF-8 core–shell structures toward $H_2$ prepared using homogeneous precipitation and screen-printing techniques.[13] Similarly, Stock *et al.* obtained ZnO@ZIF-8 composites with outstanding selectivity toward $H_2$ through ZnO transformation.[14] Additionally, Long *et al.* prepared ZnO@ZIF-8 core–shell nanorod films, while Jung *et al.* developed PMMA/ZIF-8 bilayers as molecular sieving layer with strong resistance to CO interference in $H_2$ detection.[15,16] Furthermore, Mao *et al.* fabricated flexible field-effect transistor (FET) sensors based on the *in situ* growth of $Ni_3(HHTP)_2$, which exhibited high sensitivity to $NO_2$ at room temperature (with a detection limit of 56 ppb) and excellent selectivity.[17–19] However, several notable obstacles exist. The primary issue pertains to the constrained availability of semiconductive two-dimensional (2D) MOFs featuring planar conjugated architectures, and notably, compromised conductivity due to the limited delocalized charge sources and charge transport.[20–24] The second hurdle relates to shaping those MOFs onto various solid-state substrates with great homogeneity, large-area, and even preferential orientation ascribed to the intrinsic lack of solution processability of MOFs.[25–30] Although numerous strategies have been proposed to individually address the aforementioned challenges, a straightforward approach that simultaneously bypasses these issues is highly desirable but currently absent.

Herein, we describe a straightforward template-assisted strategy to fabricate hierarchical $Ni_3(HITP)_2$/MXene heterostructures with significant conductivity, porosity, and solution processability (Fig. 1a). This method capitalizes on the 2D character and remarkable conductivity of MXene nanosheets, coupled with the lattice matching between MXene and the chosen $Ni_3(HITP)_2$. In consequence, controllable self-assembly of $Ni_3(HITP)_2$ onto MXene nanosheets was achieved, affording ultra-thin, evenly dispersed, well crystallized, and layered $Ni_3(HITP)_2$/MXene heterostructures. Three distinctive advantages can therefore be conferred. First, the resultant $Ni_3(HITP)_2$/MXene suspension demonstrates a notably improved dispersibility and thus excellent solution processability (Fig. 1b) due to their 2D nature and ultrathinness. This attribute significantly contributes to the fabrication of large-area $Ni_3(HITP)_2$/MXene films with excellent uniformity, controllable thickness, and even orientation, holding substantial potential for the scalable manufacture of advanced sensing devices. Second, the powder conductivity of the $Ni_3(HITP)_2$/MXene heterostructures experiences a notable enhancement, reaching $4.8 \times 10^3$ S $m^{-1}$, approximately 17 times greater compared to

 

that of the pristine $Ni_3(HITP)_2$. More impressively, the film conductivity of the $Ni_3(HITP)_2$/MXene heterostructure can reach $5.3 \times 10^5$ S m$^{-1}$, significantly surpassing the reported conductivity of MOF-related systems reported to date. This would unquestionably enable a heightened sensitivity in detecting targeted analytes. Third, the judicious construction of $Ni_3(HITP)_2$/MXene heterostructures witnesses the formation of strong interactions between $Ni_3(HITP)_2$ and MXene, and thus alters the intrinsic electronic structure of $Ni_3(HITP)_2$. This remarkably intensifies the efficient interaction between gas molecules and the central main-group element Ni, leading to increased sensitivity and selectivity. Gas sensors based on the $Ni_3(HITP)_2$/MXene heterostructures show remarkable sensitivity (with a limit of detection of approximately 5 ppb) and selectivity at room temperature toward ultratrace ethanol, setting a new benchmark of such gas sensors. The $Ni_3(HITP)_2$/MXene based gas sensors are tentatively utilized for real-time monitoring of human health conditions (illustrated in Fig. 1c). In comparison to the conventional method of disease diagnosis using blood samples, analyzing the respiratory gas for diagnostic purposes offers a more convenient and minimally invasive alternative. This methodology opens up novel perspectives for designing and synthesizing highly sensitive MOF-based systems, and streamlines their incorporation onto miniaturized electronic devices, paving the avenue for potential mass production.

# Experimental

### Synthesis of $Ni_3(HITP)_2$/MXene heterostructures

Nickel nitrate hexahydrate ($Ni(NO_3)_2 \cdot 6H_2O$, 50 mg) was dissolved in anhydrous ethanol (25 mL), to which concentrated ammonia solution (2 mL, 30%) was added. Meanwhile, 2,3,6,7,10,11-hexaaminotriphenylene (HITP, 33 mg) was dissolved in anhydrous ethanol (25 mL). Afterward, homogeneous solution was afforded by mixing the above two solutions. Subsequently, a dispersion of multilayered MXene ($Nb_2C$) nanosheets (5 mL) was introduced into the above mixture. $Ni_3(HITP)_2$/MXene suspensions were synthesized by incubating the resultant solution at 65 °C for 5 hours. The obtained suspension underwent five consecutive rinsing with fresh anhydrous ethanol *via* centrifugation at 8000 rpm, followed by overnight immersion in fresh anhydrous ethanol. Subsequently, the rinsed $Ni_3(HITP)_2$/MXene suspension was subjected to vacuum drying at 150 °C, resulting in the formation of $Ni_3(HITP)_2$/MXene powder.

### Fabrication of $Ni_3(HITP)_2$/MXene or MXene monodispersed nanosheets

Alcoholic $Ni_3(HITP)_2$/MXene or MXene suspension with a concentration of 0.5 g L$^{-1}$ and a volume of 20 μL was carefully deposited onto a pristine silicon wafer or a copper mesh *via* drop-casting. Subsequently, the sample was subjected to a drying process at a temperature of 80 °C for a duration of 20 minutes, effectively eliminating a significant portion of the solvent. Following this, the sample was subjected to a slow drying process under vacuum conditions for a period of one day, resulting in the production of uniformly monodispersed nanosheets of $Ni_3(HITP)_2$/MXene or MXene.

### Fabrication of $Ni_3(HITP)_2$/MXene films

$Ni_3(HITP)_2$/MXene films on small substrates were fabricated just *via* drop-casting. Typically, substrates were thoroughly rinsed by absolute ethanol twice under fierce stirring with each circle for 10 min, afterward dried at 80 °C under ambient pressure. A certain volume of $Ni_3(HITP)_2$/MXene ethanol suspension was then captured by pipette and vertically dropped onto Si surfaces. $Ni_3(HITP)_2$/MXene films can thus be formed along with the vaporization of solvent. Large-area $Ni_3(HITP)_2$/MXene films on polyvinylidene fluoride (PVDF) were fabricated by doctor-blading. Drying for all kinds of films was conducted at an ambient condition to fully vaporize the solvent, affording flat films. Further activations were done at 120 °C under vacuum. Detailed information is available in the ESI.†

### Design and fabrication of sensors

Platinum (Pt) interdigitated electrodes (IDEs) were produced and structured on silicon (Si) (100) wafers utilizing established cleanroom techniques, as documented in a previous publication.[23] The fabrication process involved precise patterning of Pt material on the Si wafers to create the interdigitated electrode configuration. Furthermore, a Pt micro-hotplate was integrated beneath the top IDEs, serving as a micro-heater. This micro-heater had the potential to activate films *in situ*. After the fabrication process, the wafers were diced into individual chips. These chips were then soldered onto printed circuit boards (PCB) to establish electrical connections. The wire coupling process, which involved connecting the IDEs to the relevant circuitry, was carried out subsequent to the soldering of the chips.

### Gas sensing measurements

The gas sensing performance of the sensors integrated with variable functionalities $Ni_3(HITP)_2$/MXene films was evaluated by measuring the resistance change before and after gas adsorption. During the measurement process, the chip was placed in a custom-made chamber with stretchable metal contacts. Before data acquisition, the chamber was purged with nitrogen ($N_2$) for 15 minutes to stabilize the baseline resistance. $N_2$ was also used as a diluent to reach the target concentration and for sensor regeneration. The flow rate of all gases was kept constant at 100 sccm. Further details can be found in the ESI.†

### Human exhaled gas detection

Human respiratory gases were collected using a breathing bag or sample collector. Participants first consumed alcohol at specified times and then exhaled into the bag or collector at designated intervals. During the measurement process, the chip was placed in a custom-made chamber with stretchable metal contacts. The collection bag containing the respiratory biomarker ethanol was connected to this chamber. The relative

changes in the target biomarker ethanol were assessed by measuring the resistance variations before and after gas adsorption. Additionally, the chamber was purged with nitrogen ($N_2$) for 15 minutes before data collection to stabilize the baseline resistance. $N_2$ was also used as a diluent to achieve the target concentration and for sensor regeneration.

### Theoretical calculations

Density functional theory (DFT) calculations were performed using the generalized gradient approximation (GGA) with the projector augmented wave (PAW) method. The Vienna *ab initio* simulation package (VASP) was employed, and a plane-wave basis set was utilized. van der Waals interactions were considered using the van der Waals density functional (vdW-DF) level with the optB86b functional (optB86b-vdW). The heterostructure consisted of a monolayer $Ni_3(HITP)_2$ and a $7 \times 7$ bilayer $Nb_2C$ superlattice, with a vacuum layer of approximately 35 Å. The lattice mismatch between $Ni_3(HITP)_2$ and the MXene was less than 0.7%. During structural relaxations, all atoms were fully relaxed until the residual force on each atom was less than 0.05 eV $Å^{-1}$. The kinetic energy cutoff for the plane-wave basis was set to 500 eV. The adsorption energy ($E_{ads}$) was calculated as follows: $E_{ads} = E_{molecule+substrate} - E_{substrate} - E_{molecule}$, where $E_{molecule+substrate}$ represents the total energy of the adsorption geometry, and $E_{substrate}$ and $E_{molecule}$ are the energies of the individual substrate and the isolated molecule, respectively.

### Characterizations

Fourier-transform infrared (FTIR) patterns were obtained by a Nicolet iS50 FTIR spectrometer. XPS spectrum obtained by ESCALAB $Xi^+$ X-ray photoelectron spectroscopy. Microstructural characterizations of $Ni_3(HITP)_2$/MXene nanosheets and relevant films, were characterized by scanning electron microscopy (SEM, SU8230) and X-ray diffractometer (XRD, Bruker) equipped with Cu Kα radiation ($\lambda = 1.5406$ Å) under a Bragg–Brentano geometry with a step size of 0.02° and a scan speed of 0.5° $min^{-1}$. Two-dimensional (2D) grazing-incidence wide-angle X-ray scattering (GIWAXS) measurements were performed on Nanoinxider (Xenocs) with Cu Kα radiation as the source at an incidence angle of 0.2°. Transmission electron microscopy (TEM) imaging was conducted *via* a JEOL TEM (JEM-2100). High angle annular dark field (HAADF)-STEM imaging was performed by a JEM-ARM200F (JEOL) microscope equipped with an ASCOR aberration corrector and a cold-field emission gun, operated at 200 kV. Atomic force microscopy (AFM) with tapping mode was used for imaging $Ni_3(HITP)_2$/MXene and MXene nanosheets or films at room temperature. $N_2$ sorption isotherms were collected under 77 K using a Micromeritics ASAP 2460 surface area and pore size analyzer. Conductivity of $Ni_3(HITP)_2$/MXene and MXene powder and films were measured using the standard four electrode method.

## Results and discussion

The typical synthesis of $Ni_3(HITP)_2$/MXene heterostructures involves the use of template-assisted growth approach. Specifically, facile solvothermal incubation of ethanol solutions containing $Ni(NO_3)_2 \cdot 6H_2O$ (4.362 g $L^{-1}$), HITP·6HCl (5.371 g $L^{-1}$), ammonia (30%) and multilayered MXene (5 g $L^{-1}$) nanosheets at 65 °C leaded to the formation of black viscous suspensions. The nucleation and growth of $Ni_3(HITP)_2$ on MXene nanosheets can be verified by several techniques. Scanning electron microscopy (SEM) imaging confirms the 2D characteristics of the resultant structures (Fig. 2a), which were obtained by drop-casting a diluted suspension onto an atomically flat silicon (Si) surface. Zoomed-in SEM images indicate the formation of compact $Ni_3(HITP)_2$ layer with protruding large crystal islands (Fig. 2b, S1 and S2, ESI†). Energy dispersive spectroscopy (EDS) line scanning reveals the characteristic Ni element distribution within $Ni_3(HITP)_2$ at the periphery of the $Ni_3(HITP)_2$/MXene heterostructure (Fig. 2c and S3 in the ESI†). A noticeable gradient change in Ni element content was observed at the edge of the heterostructure, with significantly elevated levels within the $Ni_3(HITP)_2$-present region. This observation further corroborates the formation of $Ni_3(HITP)_2$ on the MXene nanosheets, thereby substantiating the successful construction of the $Ni_3(HITP)_2$/MXene heterostructure. The low-magnification transmission electron microscopy (TEM) image (Fig. 2d and S4 in the ESI†) also captures the 2D crystallographic attributes of the $Ni_3(HITP)_2$/MXene heterostructure. The elemental mapping image (Fig. S5, ESI†) underlines the concentrated aggregation of $Ni_3(HITP)_2$ crystals on the MXene nanosheets, with growth occurring likely on both sides of the MXene nanosheet, consistent with the corresponding SEM images. Furthermore, the high-angle annular dark-field scanning transmission electron microscopy (HAADF-STEM) image of these nanosheets (Fig. 2e and S6 in the ESI†) suggests the unambiguous presence of lattice fringes with a representative interplanar spacing of 2.0 nm that corresponds to the (100) plane of $Ni_3(HITP)_2$. Detailedly, distinct hexagonal lattice points denoting Ni atoms were prominently discerned (Fig. S6 in the ESI†), exhibiting an interspace of 2.0 nm between adjacent pore centers. This observation consistently aligns with the crystal structure and matches well with the theoretical atomic model as previously reported.[21] The formation of $Ni_3(HITP)_2$ on the MXene nanosheets can also be reflected by X-ray Photoelectron Spectroscopy (XPS) and Fourier transform infrared (FTIR) (Fig. S7 and S8, ESI†). The height profile, extracted from atomic force microscopy (AFM) images (Fig. 2f, g, S9 and S10 in the ESI†), unveils that the MXene nanosheets possesses an average thickness of approximately 3 nm. Meanwhile, the averaged thickness of the $Ni_3(HITP)_2$/MXene heterostructure is about 15 nm, with the $Ni_3(HITP)_2$ layer atop the MXene surface contributing roughly 6 nm. In contrast, within the control experiment conducted under identical conditions but without MXene as the template, $Ni_3(HITP)_2$ crystals exhibits a random distribution lacking orientation (Fig. S11 in the ESI†). This highlights the indispensable role of MXene during the *in situ* growth of $Ni_3(HITP)_2$.

Additionally, the powder X-ray diffraction (PXRD) spectra (Fig. 2h) reveals that the pattern of the synthesized $Ni_3(HITP)_2$/MXene is highly consistent with that of $Ni_3(HITP)_2$ simulated from its crystal structure, definitively confirming the successful

 

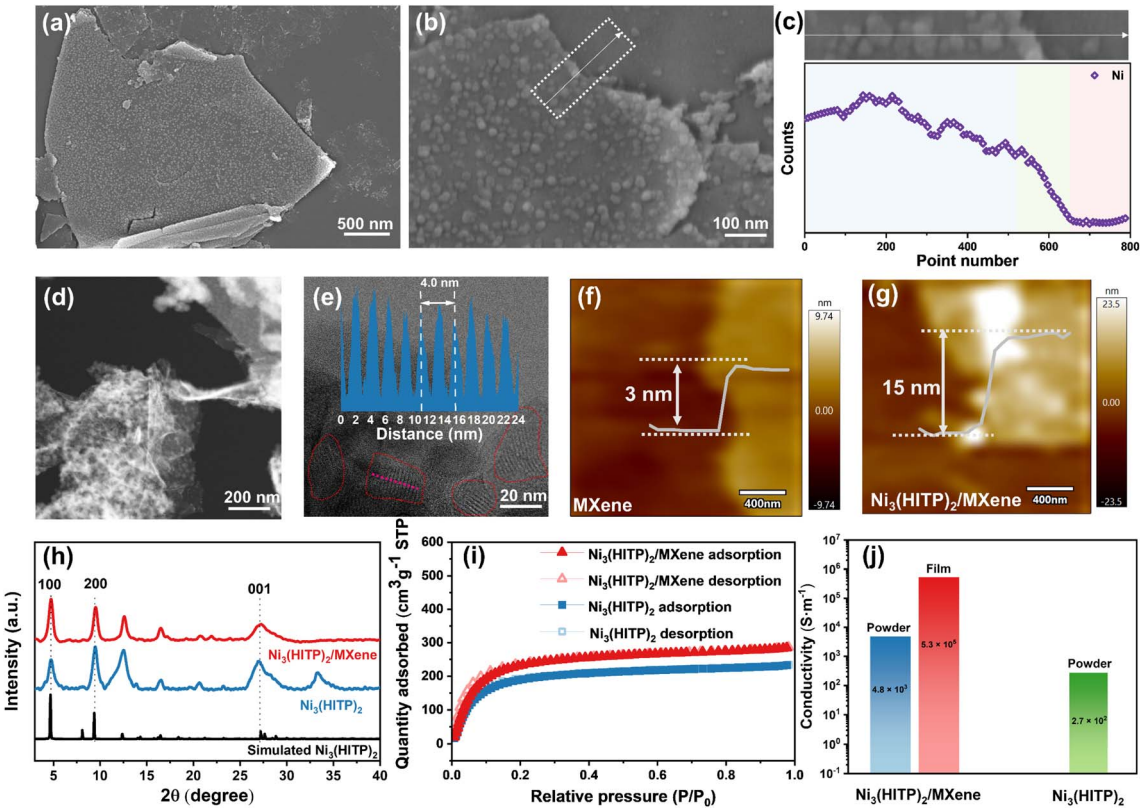


Fig. 2 Structure and morphological characterization of $Ni_3(HITP)_2$/MXene heterostructure. (a and b) SEM images of $Ni_3(HITP)_2$/MXene nanosheets deposited on silicon surfaces. (c) Energy-dispersive X-ray spectroscopy (EDS) showing the spatial distribution of the distinctive Ni element within the edge region of the $Ni_3(HITP)_2$ region of the $Ni_3(HITP)_2$/MXene heterostructure. (d) Low-magnification TEM image of $Ni_3(HITP)_2$/MXene nanosheets. (e) HAADF-STEM image of the $Ni_3(HITP)_2$/MXene nanosheet. The inset in (e) shows the intensity line profile of the lattice indicated by the purple dashed lines. (f and g) AFM images of MXene and $Ni_3(HITP)_2$/MXene nanosheets. (h and i) XRD patterns and $N_2$ adsorption isotherms of $Ni_3(HITP)_2$/MXene and $Ni_3(HITP)_2$ powders at 77 K, in comparison with the theoretical XRD pattern of $Ni_3(HITP)_2$ powder. (j) Comparison chart of electrical conductivity between $Ni_3(HITP)_2$/MXene powder pellet and thin film, as well as with the $Ni_3(HITP)_2$ powder pellet.

growth of $Ni_3(HITP)_2$ on MXene surfaces. The adsorption–desorption isotherms of the resultant $Ni_3(HITP)_2$/MXene and $Ni_3(HITP)_2$ were derived from nitrogen ($N_2$) sorption measurements conducted at 77 K. These profiles, illustrated in Fig. 2i, adhered to type I isotherms, indicative of the micropore filling behavior observed during gas adsorption. The Brunauer–Emmett–Teller (BET) surface area of $Ni_3(HITP)_2$ was calculated to be 633.5 $m^2\ g^{-1}$ by fitting the sorption curves, which is comparative to the reported value.[4] In stark contrast, the BET surface area of $Ni_3(HITP)_2$/MXene was quantified to be 797.8 $m^2\ g^{-1}$, representing a substantial enhancement. Moreover, the predominant pore size, primarily centered around 2 nm as illustrated in Fig. S12 of the ESI,† align with that of its the crystal structure.[21] The apparent augmentation in specific surface area is beneficial to the enhancement of gas adsorption capacity and gas diffusion, and also provides more active sites for ample gas–surface interaction and/or reaction, thereby contributing to enhanced gas sensing performance. The powder conductivity of the $Ni_3(HITP)_2$/MXene heterostructure was derived to be $4.8 \times 10^3$ S $m^{-1}$ using the standard four-electrode method (Fig. 2j and S13, ESI†), which is around 17.9 times higher than that of the original $Ni_3(HITP)_2$ ($2.7 \times 10^2$ S $m^{-1}$). It is noteworthy that the $Ni_3(HITP)_2$/MXene heterostructure exhibits excellent film-forming properties, resulting in a remarkable thin film conductivity of up to $5.3 \times 10^5$ S $m^{-1}$. In contrast, the film produced by $Ni_3(HITP)_2$ alone possesses a significantly lower conductivity of around 1.2 S $m^{-1}$. This inferior conductivity can be attributed to its non-compactness and discontinuity due to the severe agglomeration of $Ni_3(HITP)_2$ nanoparticles, falling even below the steady-state powder pellet conductivity. By incorporating MXene nanosheets and enabling the controllable *in situ* growth of $Ni_3(HITP)_2$, the resultant $Ni_3(HITP)_2$/MXene heterostructure exhibits notably elevated conductivity when compared to both pure MOFs and the majority of MOF-based composite materials[31–41] (as documented in Table S1 of the ESI†). The remarkable conductivity and sheet-like nanostructure of the $Ni_3(HITP)_2$/MXene heterostructures with a large specific surface area likely play a pivotal role in achieving an unparalleled electrical sensitivity to guest molecules.[27] These attributes undoubtedly make this heterostructure well-suited for chemiresistive gas sensing with outstanding sensing performance.

Fabricating MOFs with hierarchical pore structures is highly desirable for expanding their industrial applicability. The direct

usage of micro/nano MOF powders brings a range of technical obstacles, including suboptimal manipulability, constrained mass transport, generation of dust, and undesired pressure drops within packed beds.[42–45] To overcome these challenges, synthesis of solution processable MOF-based suspensions are highly expected. Consequently, they can be processed into uniformly and densely films with controllable thickness using various solution processing techniques such as drop-casting, spin-coating, and doctor-blading.[46–51] Visual examination of $Ni_3(HITP)_2$/MXene, $Ni_3(HITP)_2$, and MXene/$Ni_3(HITP)_2$ mixture suspensions before and after a five day quiescence at room temperature depicted in Fig. 3a, b and S14,† unveiled notable sedimentation in the cases of $Ni_3(HITP)_2$ and of the direct mixture of MXene with $Ni_3(HITP)_2$. In contrast, the $Ni_3(HITP)_2$/MXene suspension sustained excellent solution dispersibility and stability over the same duration. Leveraging the good solution processability of the resulting $Ni_3(HITP)_2$/MXene suspensions, a series of uniform and dense $Ni_3(HITP)_2$/MXene films with controllable thickness can be facilely prepared on variable solid-state substrates *via* drop-casting (Fig. 3c–f and S15–S17, ESI†). Impressively, the excellent fluidic properties of the $Ni_3(HITP)_2$/MXene suspensions also endows the fabrication of large-area films with good homogeneity and compactness. Fig. 3g depicts the digital photograph of the large-area $Ni_3(HITP)_2$/MXene film on polyvinylidene fluoride (PVDF) substrate fabricated by doctor-blading. Rigorous bending assessments conducted on the flexible PVDF substrates underscored their robustness and manufacturability. The discernible variation in

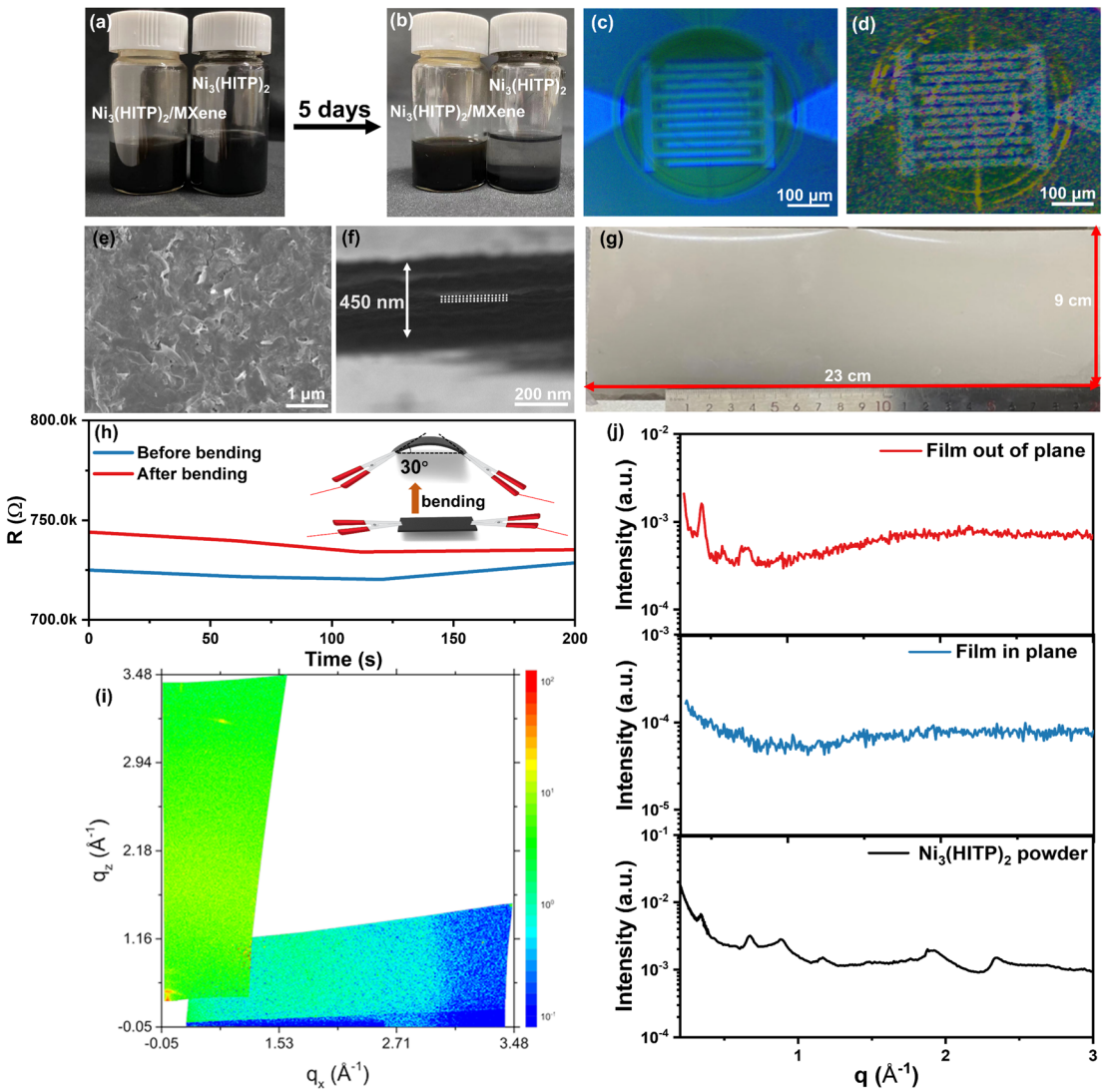


Fig. 3 Morphological characterization of $Ni_3(HITP)_2$/MXene thin films. (a and b) Optical photographs of $Ni_3(HITP)_2$/MXene and $Ni_3(HITP)_2$ suspensions both prior to and after being left at room temperature for a duration of five days. (c and d) Optical photographs of the sensor before and after $Ni_3(HITP)_2$/MXene coating. (e) Representative top-view SEM image of $Ni_3(HITP)_2$/MXene film. (f) Cross-sectional SEM image of the film as shown in (e). (g) Optical photograph of a large-area $Ni_3(HITP)_2$/MXene film prepared on a polyvinylidene fluoride (PVDF) substrate by doctor-blading. $C_{Ni_3(HITP)_2/MXene} = 5$ g $L^{-1}$, volume = 8 mL. (h) Real-time resistance of the $Ni_3(HITP)_2$/MXene film before and after bending at 30 degrees. Inset depicts the testing configuration. (i) 2D-GIWAXS image of the prepared $Ni_3(HITP)_2$/MXene film. (j) Comparison of the out-of-plane and in-plane GIWAXS scattering profiles of the $Ni_3(HITP)_2$/MXene film with the $Ni_3(HITP)_2$ powder form.

 

film conductivity before and after bending, as illustrated in Fig. 3h and S18 in the ESI,† further highlights their potential usage for flexible electronics. It is important to highlight that a noticeable trend of resistance signal overlap emerges between the bent and unbent films after approximately 200 seconds. We postulate that this overlapping pattern can be attributed to both the stress applied by the testing fixture to the flexible substrate and the gradual stress recovery of the flexible substrate following bending, thereby enabling partial restoration of the conductive pathway. Additional bending tests toward the films at variable angles indicate that the $Ni_3(HITP)_2$/MXene films at lower bending angles witnessed nearly unchanged morphologies in comparison with their pristine state (Fig. S19†). However, after having underwent significant bending (larger than 60°), tiny cracks did appear within the $Ni_3(HITP)_2$/MXene film. These cracks may probably result from the inherent brittleness of $Ni_3(HITP)_2$/MXene and additional stress induced by bending.

Furthermore, 2D grazing incidence wide-angle X-ray scattering (GIWAXS) measurements were conducted to investigate the crystallinity and orientation of the relevant films (Fig. 3i, j and S20, ESI†). Of particular note, out-of-the plane measurements of the $Ni_3(HITP)_2$/MXene film revealed that nearly most of the peaks matched with those of the pure $Ni_3(HITP)_2$ powder, albeit with significantly increased peak intensities. This discovery implies that the incorporation of MXene nanosheets yields a favorable enhancement in the crystallinity of $Ni_3(HITP)_2$ and emphasizes the indispensable role of MXene nanosheets as the template. The absence of noticeable out-of-plane orientation is likely attributed to the inclined disposition of $Ni_3(HITP)_2$/MXene nanoplatelets on the surface and the weak interlayer stacking between adjacent layers. Additionally, the resultant $Ni_3(HITP)_2$/MXene film also lacks notable in-plane peaks, indicating the absence of any distinct in-plane preferential orientation. Thus, we postulate that the $Ni_3(HITP)_2$/MXene nanoplatelets may be tilted relative to the substrate, affording them not only vertically-oriented 1D channels but also an enlarged contact area with gas molecules, both of which are highly advantageous for gas adsorption.[46,47]

Miniaturized gas sensors based on the resultant $Ni_3(HITP)_2$/MXene heterostructures with a thickness of approximately 450 nm were successfully fabricated by combining $Ni_3(HITP)_2$/MXene nanosheets with interdigitated electrodes (IDEs) (Fig. 3f and S22, ESI†), and their chemiresistive sensing performance was fully evaluated using a custom-designed gas detection setup (Fig. S21, ESI†). Detailedly, the resistance of the $Ni_3(HITP)_2$/MXene layer on IDEs changes in response to different gas types and concentrations. By monitoring the resistance changes of the $Ni_3(HITP)_2$/MXene coated gas sensors, the concentration and even the type of related gases can thus be reflected.[41–43] Fig. 4a and b illustrate dynamic response–recovery curves of the $Ni_3(HITP)_2$/MXene coated gas sensors at room temperature upon exposure to variable concentrations of ethanol (EtOH) and ammonia ($NH_3$) ranging from 1 to 10 parts per million (ppm). The curves illustrate a notable response in resistance upon exposure to variable concentrations of EtOH and $NH_3$; and the reversible alterations nearly remained consistent across three cycles. To further evaluate the sensor's performance in low concentration atmospheres, we recorded the response–recovery curve for EtOH in the range of 100 parts per billion (ppb) to 1.5 ppm (Fig. 4c). Notably, even at an EtOH concentration as low as 100 ppb, we observed an obvious response of approximately 0.28%. This level of sensitivity surpasses gas sensors relying on pure MOFs or MOF-based composites, and most metal oxide semiconductors (MOS) (Table S2, ESI†) from the literature.

To investigate the sensing process in detail, the response time, representing the duration required to induce 90% resistance variation of its saturation value, was estimated to be 120 seconds for 10 ppm of EtOH, while the recovery time, necessary to recover to 10% of the original value, was found to be around 65 seconds (Fig. 4d). These values indicate fast response and recovery of the $Ni_3(HITP)_2$/MXene based gas sensors and represent an improvement of 35.1% and 32.2%, respectively, compared to those of the sensors based on $Ni_3(HITP)_2$ powder (Fig. S23, ESI†). The addition of MXene enhanced the film quality and conductivity, leading to faster response. By examining the linear plotting depicting the response of the $Ni_3(HITP)_2$/MXene and $Ni_3(HITP)_2$ sensors to EtOH and $NH_3$ concentrations (Fig. 4e and f), we observed that the $Ni_3(HITP)_2$/MXene coated sensors exhibited significantly improved response compared to that of the sensors based on $Ni_3(HITP)_2$. The $Ni_3(HITP)_2$/MXene coated sensors demonstrated superior gas sensitivity, primarily attributed to the synergistic effect of the $Ni_3(HITP)_2$/MXene heterostructure. Based on the data from Fig. 4d and e and the root mean square deviation,[52] we computed the limit of detection (LOD) of the $Ni_3(HITP)_2$/MXene coated sensors for $NH_3$ and EtOH, which were determined to be 250 ppb and 5 ppb, respectively. It's noteworthy to highlight that the controllable growth of $Ni_3(HITP)_2$ crystals on the MXene surface played a pivotal role in achieving such remarkably low detection limits. In a control experiment utilizing the $Ni_3(HITP)_2$ alone, the corresponding devices could scarcely detect $NH_3$ and EtOH molecules when their concentrations fall below 1 ppm (Fig. S24, ESI†).

Additionally, the $Ni_3(HITP)_2$ coated sensors exhibit distinct cross-sensitivity at room temperature to reducing gases, *i.e.*, acetone, formaldehyde, and carbon monoxide, as shown in Fig. 5a, b and S25–S30 (ESI),† but with all responses below 7%. In contrast, the $Ni_3(HITP)_2$/MXene coated sensors exhibit not only enhanced response to various reducing gases but also demonstrate excellent selectivity toward ethanol. Compared to the MXene coated sensors with negligible response toward ethanol (Fig. S31, ESI†), the $Ni_3(HITP)_2$/MXene coated sensors showed significantly improved capability to distinguish ethanol from other gases. To evaluate the anti-interference capability of the $Ni_3(HITP)_2$/MXene-coated sensor, we conducted extensive tests in mixed gas environments featuring different concentrations (1, 5, 9 ppm) and various gas types (ethanol, acetone, formaldehyde, carbon monoxide, ammonia, water vapor), as illustrated in Fig. S32 and S33 in the ESI.† The results demonstrated that even at a concentration as low as 1 ppm of ethanol in the mixed gas, the sensors manifested a noticeable response. The correlation heatmap (Fig. 5c) clearly indicated the absence of any significant correlations between the gas response and

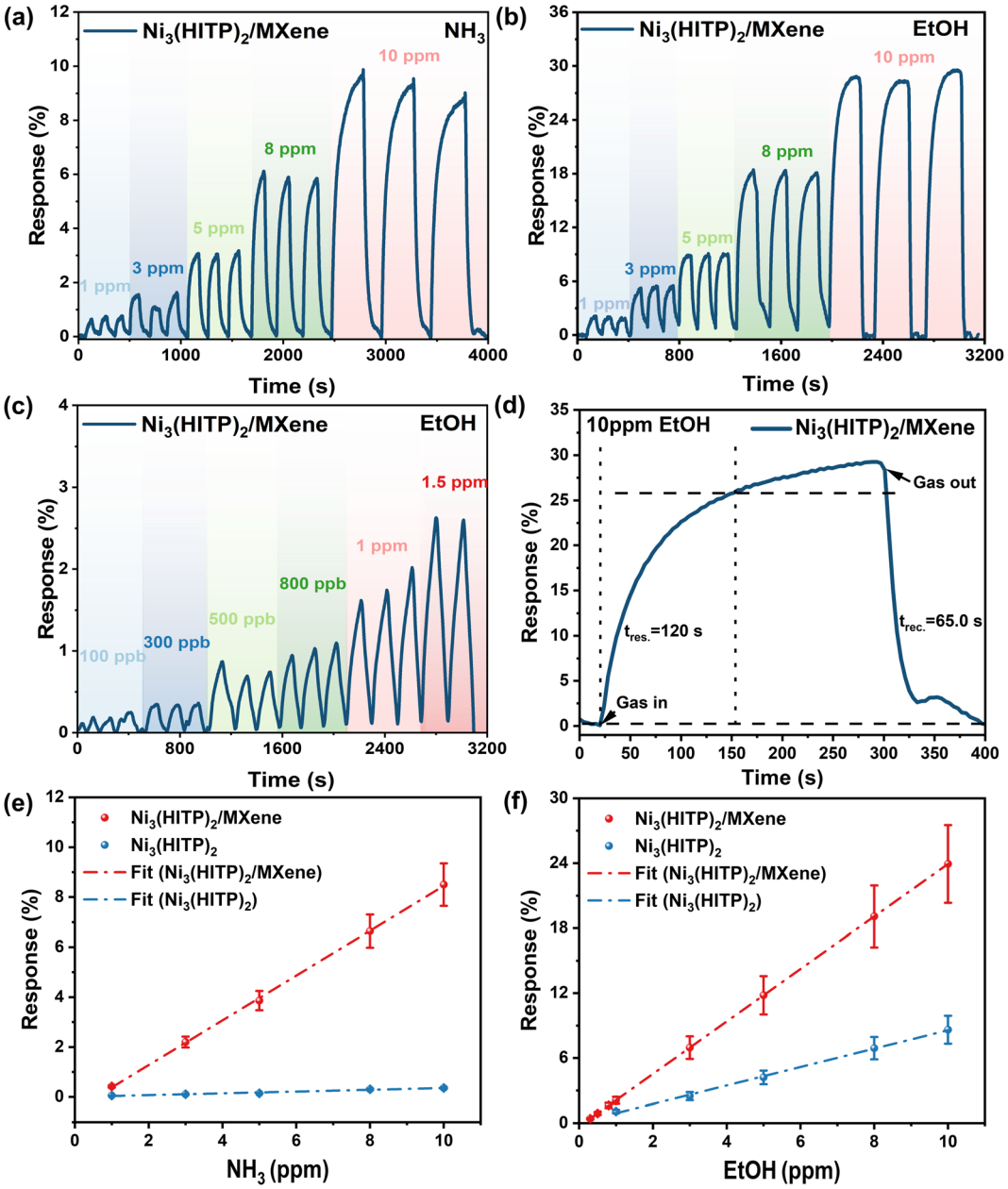


Fig. 4 Gas response performance of $Ni_3(HITP)_2$/MXene sensors at room temperature. (a and b) Response–recovery curves of the $Ni_3(HITP)_2$/MXene coated sensors to different concentrations of $NH_3$ and EtOH. (c) Response–recovery curve of $Ni_3(HITP)_2$/MXene coated sensor toward low concentration of EtOH. (d) Zoomed-in response–recovery time curves of the $Ni_3(HITP)_2$/MXene coated sensor to 10 ppm EtOH. (e and f) Linear plots of response *versus* concentration of EtOH and $NH_3$ for $Ni_3(HITP)_2$/MXene and $Ni_3(HITP)_2$ sensors. The individual data points represent the experimental observations (the number of reference samples for the error bar is 5), and the continuous pink lines represent the linear fittings.

acetone, formaldehyde, carbon monoxide, ammonia, or water vapor. However, it revealed a strong correlation with ethanol, suggesting selective detection toward ethanol. Additionally, the $Ni_3(HITP)_2$/MXene coated sensors showed relatively good long-term stability, preserving nearly 80% of its initial response to 1 ppm ethanol even after 150 days (Fig. 5d and S34 in the ESI†). This is advantageous for practical use in environmental conditions over extended periods. Compared with other ethanol gas sensors based on pure MOFs or MOF-based composites, and most metal oxide semiconductors (MOS) from the literature,[27,31–33,35,36,40,44,52–57] the $Ni_3(HITP)_2$/MXene based sensors exhibit superior sensing performance at room temperature in terms of sensitivity and selectivity (Fig. 5e and Table S2 in the ESI†).

Subsequently, we tentatively utilized the sensors as integral components for continuous gas monitoring at room temperature, with a specific focus on monitoring human health status. In this context, we recorded real-time resistance changes in

 

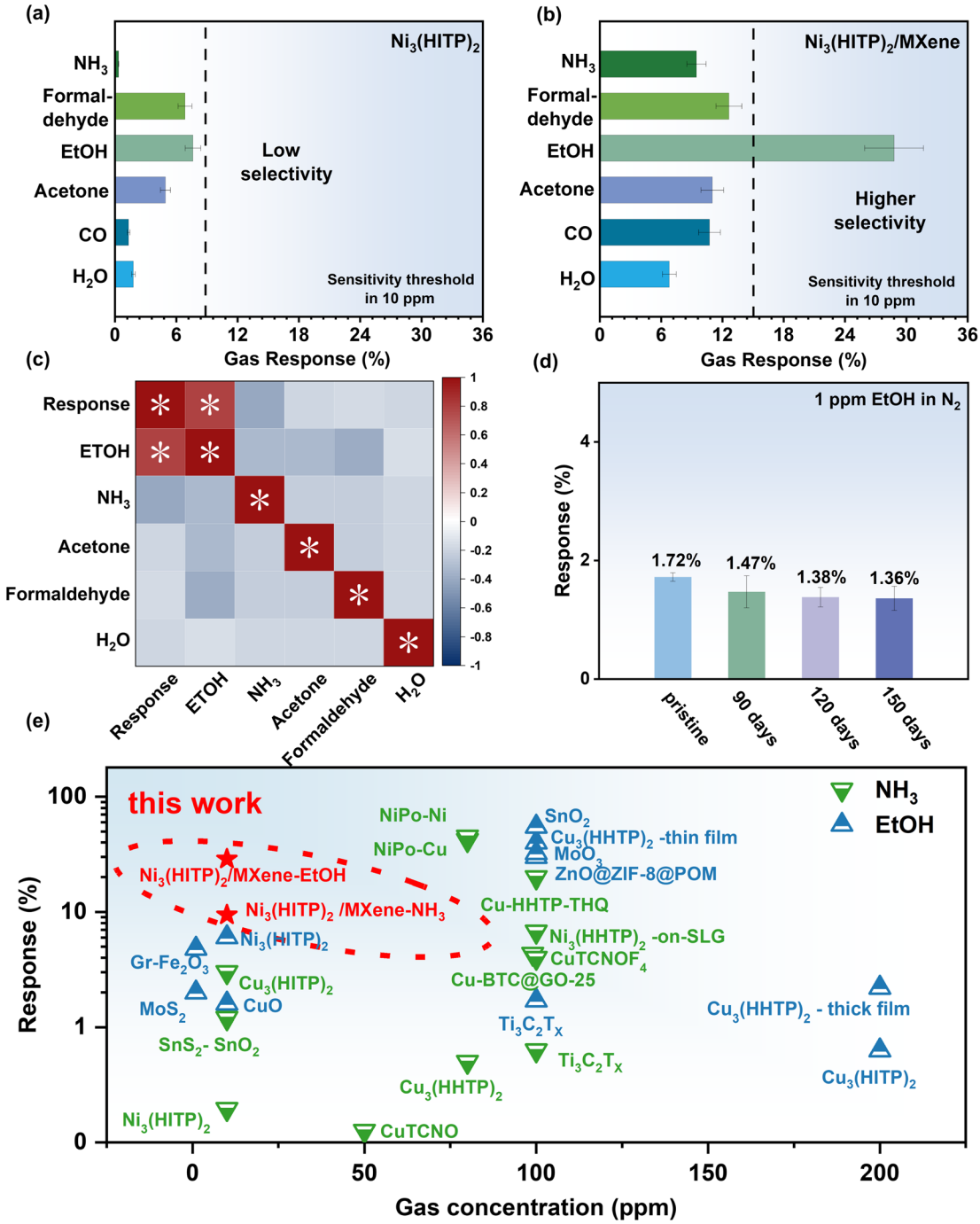


Fig. 5 Gas sensing performance of $Ni_3(HITP)_2$/MXene-coated sensors. (a and b) Response bar charts of the sensors based on $Ni_3(HITP)_2$/MXene and $Ni_3(HITP)_2$ to different reducing gases, respectively. (c) Correlation heatmap of the $Ni_3(HITP)_2$/MXene coated sensor upon response to mixed gases containing different reducing gases, $P < 0.05$. (d) Relatively long-term stability of the $Ni_3(HITP)_2$/MXene coated sensor to 1 ppm EtOH. (e) Sensing performance comparison of the $Ni_3(HITP)_2$/MXene coated sensor toward EtOH and $NH_3$ with those of gas sensors based on pure MOF or MOF-based composite materials, and MOS-based gas sensors reported in the literature.

response to human breath over a span of 24 hours after alcohol consumption (Fig. S35–S37 in the ESI†). The results revealed that within just 40 minutes after drinking, significant alterations in breath response occurred when compared to the baseline, signaling the onset of a state of inebriation (Fig. S37†). Over the ensuing 3–5 hours, the breath response exhibited a gradual stabilization, mirroring the individual's shift from a state of intoxication to one of mild inebriation. Ultimately, between the 12–24 hours, the breath response closely resembled that of the baseline, signifying the person's return to a normal state. It's important to highlight that typical breath composition indeed

elicits a specific response, potentially attributed to the interference from water vapor or other gases present in exhaled breath.

Density functional theory (DFT) calculations were carried out to understand the sensing mechanism of sensors based on $Ni_3(HITP)_2$/MXene heterostructures. We built a heterostructure composed of a monolayer $Ni_3(HITP)_2$ and a $7 \times 7$ bilayer MXene superlattice, as depicted in Fig. S38.† The heterostructure displays a strong interlayer interaction, as evidenced by a smaller interlayer distance of ~2.1 Å and a lower interlayer binding energy of −0.07 eV $Å^{-2}$. Fig. 6a shows interlayer differential charge density (DCD) and line profile between $Ni_3(HITP)_2$ and MXene. The MXene substrate had a profound impact on the charge distribution within $Ni_3(HITP)_2$. Electrons were transferred from MXene to $Ni_3(HITP)_2$, with interlayer electrons accumulating predominantly on the lower surface of the $Ni_3(HITP)_2$ framework. This robust charge transfer resulted in a notable enhancement of interlayer coupling.[58–62] According to Bader charge analysis results, the Ni, N, and C atoms within the $Ni_3(HITP)_2$/MXene heterostructure increased by an average of 0.23*e*, 0.07*e*, and 0.21*e*, respectively. Electropositivity and electronegativity of Ni and C atoms in $Ni_3(HITP)_2$ framework were effectively modulated by MXene. It is worth noting that, as depicted in the ultraviolet-visible (UV-vis) spectra of $Ni_3(HITP)_2$ and $Ni_3(HITP)_2$/MXene samples (Fig. S39 and S40, ESI†), the calculated band gaps for $Ni_3(HITP)_2$ and $Ni_3(HITP)_2$/MXene stand at 2.57 eV and 1.85 eV, respectively. This suggests that the strong interlayer interaction between $Ni_3(HITP)_2$ and MXene reduced the band gap of $Ni_3(HITP)_2$/MXene, thereby facilitating electron transitions from the valence band to the conduction band.

Moreover, Fourier-transform infrared spectroscopy (FTIR) was used to examine the $Ni_3(HITP)_2$/MXene heterostructures before and after adsorption of EtOH (Fig. 6b and S41, ESI†). The presence of distinctive peaks at 2960, 1043, and 856 $cm^{-1}$ for EtOH–Ni signifies interactions between ethanol and the $Ni_3(HITP)_2$ skeleton.[26] Furthermore, the observation of characteristic –OH vibration at 3296 $cm^{-1}$ and the red shift of $\nu$(C–N) from 1230 to 1274 $cm^{-1}$ in the vicinity of Ni suggests the potential presence of interaction between ethanol and the carbon atoms of $Ni_3(HITP)_2$.[28] Additionally, X-ray photoelectron spectroscopy (XPS) was employed to scrutinize the chemical environment of Ni sites both before and after EtOH adsorption,

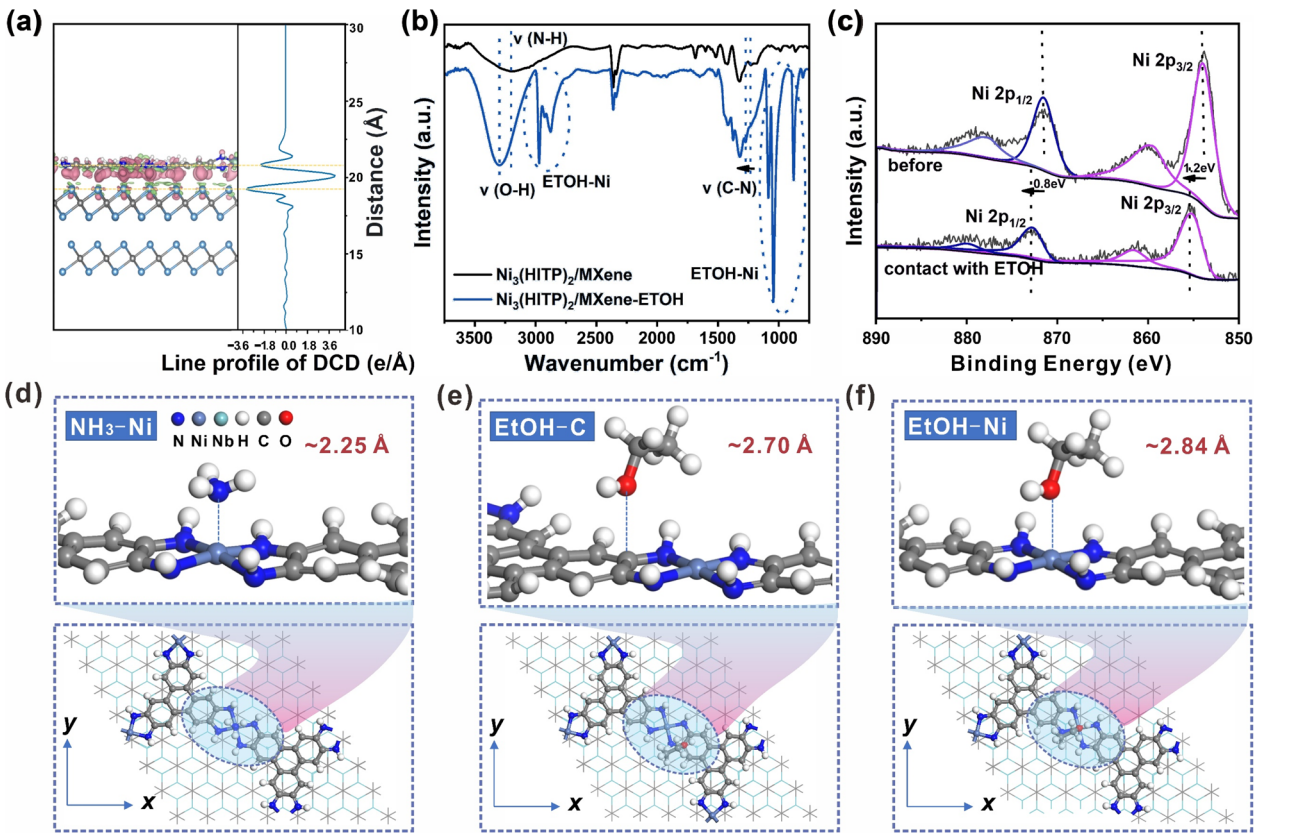


Fig. 6 Gas sensing mechanism of $Ni_3(HITP)_2$/MXene (a) differential charge density plots of $Ni_3(HITP)_2$/MXene heterostructure and the corresponding line profile along *z* axis (10–30 Å). Isosurface value is 0.008 e $Å^{-3}$, the red region denotes electron accumulation while green represents electron depletion. (b and c) FTIR and XPS spectra of the $Ni_3(HITP)_2$/MXene powder before and after adsorption of EtOH at a relatively high concentration (1000 ppm). (d–f) Geometrically optimized structures of $NH_3$ and EtOH physisorpted on $Ni_3(HITP)_2$/MXene heterostructures. The configurations of $NH_3$ adsorbed on the Ni site and ETOH adsorbed on C/Ni sites in the top view are shown in the bottom panel, respectively. The oval section in the side view is shown in the corresponding top panel. The darker blue to light blue represent N, Ni and Nb atoms; H, C, O atoms are depicted using white, gray and red balls.

 

as depicted in Fig. 6c. Upon contact with EtOH, noteworthy shifts of 1.2 eV for the Ni $2p_{3/2}$ peak and 0.8 eV for the Ni $2p_{1/2}$ peak were observed, suggesting potential interaction between the Ni site within the $Ni_3(HITP)_2$ framework and the adsorbed EtOH.[58] Those spectroscopic investigations provide insights into the interaction between the $Ni_3(HITP)_2$/MXene heterostructure and gas molecules, wherein interactions may form at the Ni and C sites of $Ni_3(HITP)_2$ and EtOH.

We conducted a theoretical investigation of the adsorption of CO, $NH_3$, and EtOH on both Ni and C sites of $Ni_3(HITP)_2$. In all configurations, the interaction between the gas molecules and $Ni_3(HITP)_2$ was notably augmented by the presence of MXene (Fig. 6d–f, S42 and Table S3, ESI†). Significantly, the $Ni_3(HITP)_2$/MXene heterostructure exhibited a notably stronger interaction with EtOH in comparison to other gases, aligning with the gas sensing data. These observations collectively supported the outstanding sensitivity and selectivity toward EtOH.

## Conclusions

In summary, we described an alternative approach for constructing solution processable $Ni_3(HITP)_2$/MXene heterostructures with respective powder and film conductivity of $4.8 \times 10^3$ and $5.3 \times 10^5$ S $m^{-1}$ and high porosity (BET surface area of 797.8 $m^2$ $g^{-1}$) *via* a facile template approach. This method leverages the 2D nature and excellent conductivity of MXene nanosheets, along with the lattice matching between MXene and selected $Ni_3(HITP)_2$, to achieve the controllable self-assembly of $Ni_3(HITP)_2$ on MXene sheets. The resultant outstanding solution processability facilitates the production of large-area (23 cm × 9 cm) $Ni_3(HITP)_2$/MXene films with good uniformity and their facile integration onto miniaturized gas sensors with potential mass production. The $Ni_3(HITP)_2$/MXene coated sensors demonstrated remarkable sensitivity (LOD ~ 5 ppb) and selectivity towards ultra-trace ethanol at room temperature, setting a new benchmark for ethanol sensors reported from the literature. This superior sensing performance is attributed to charge redistribution within the $Ni_3(HITP)_2$/MXene heterostructures and enhanced interactions between the $Ni_3(HITP)_2$/MXene and EtOH, as confirmed by experimental results and theoretical calculations. Tentative real-time respiratory gas sensing measurements further validate their underlying suitability for healthcare monitoring. This straightforward approach promises to simplify the incorporation of MOF-related functional materials with optimal conductivity, porosity, and solution processability onto miniaturized electronic devices, enabling potential mass production and exceptional performance.

## Author contributions

H. Y. conceived and designed the project. X. W. conducted the experiments, analyzed the data and drafted the manuscript. M. N. J. Q. X. W. Y. W. and W. J. performed the calculations. X. T. and J. T. contributed to the fabrication of chips. X. P. Y. L. S. X. and M. Z. contributed to the discussion of gas sensing tests. P. J. S. B. performed the GIWAXS measurements and helped on plotting the curve. All the authors have contributed to the revision of the manuscript.

## Conflicts of interest

The authors declare the following competing financial interest(s): a patent has been filed by China National Intellectual Property Administration based on the present results (Application No. 202310583388.1).

## Acknowledgements

This work was supported by the National Natural Science Foundation of China (22201226 and 12374170). H. Y. is also grateful to the support from "High-Level Overseas Talent Returning to China" project, High-level Young Talent Recruiting Plan of Shaanxi Province, and the support from Xi'an Jiaotong University within the framework of the "Young Talent Support Plan". We are also grateful to the supports from Instrumental Analysis Center of Xi'an Jiaotong University, Prof. Jiangjing Wang, and Chao Nie and for the technical support.

## Notes and references

1 W. T. Koo, J. S. Jang and I. D. Kim, *Chem*, 2019, **5**, 1938–1963.
2 H. Li, S. Zhao, S. Zang and J. Li, *Chem. Soc. Rev.*, 2020, **49**, 6364–6401.
3 R. A. Potyrailo, *Chem. Rev.*, 2016, **116**, 11877–11923.
4 M. Yao, W. Li and G. Xu, *Coord. Chem. Rev.*, 2021, **426**, 213479.
5 M. C. Wang, R. H. Dong and X. L. Feng, *Chem. Soc. Rev.*, 2021, **50**, 2764–2793.
6 N. Giri, C. E. Davidson, G. Melaugh, M. G. Del Pópolo, J. T. A. Jones, T. Hasell, A. I. Cooper, P. N. Horton, M. B. Hursthouse and S. L. James, *Chem. Sci.*, 2012, **3**, 2153–2157.
7 N. Giri, M. G. Del Pópolo, G. Melaugh, R. L. Greenaway, K. Rätzke, T. Koschine, L. Pison, M. F. C. Gomes, A. I. Cooper and S. L. James, *Nature*, 2015, **527**, 216–220.
8 A. Bavykina, A. Cadiau and J. Gascon, *Coord. Chem. Rev.*, 2019, **386**, 85–95.
9 J. R. Li, R. J. Kuppler and H. C. Zhou, *Chem. Soc. Rev.*, 2009, **38**, 1477–1504.
10 J. Liu, L. Chen, H. Cui, J. Zhang, L. Zhang and C. Y. Su, *Chem. Soc. Rev.*, 2014, **43**, 6011–6061.
11 W. Cai, J. Wang, C. Chu, W. Chen, C. Wu and G. Liu, *Adv. Sci.*, 2019, **6**, 1801526.
12 M. S. Yao, K.-i. Otake, J. Zheng, M. Tsujimoto, Y. F. Gu, L. Zheng, P. Wang, S. Mohana, M. Bonneau, T. Koganezawa, T. Honma, H. Ashitani, S. Kawaguchi, Y. Kubota and S. Kitagawa, *Angew. Chem., Int. Ed.*, 2023, **62**, e202303903.
13 R. Lv, Q. Zhang, W. Wang, Y. Lin and S. Zhang, *Sensors*, 2021, **21**, 4069.

14 M. P. M. Poschmann, L. Siebert, C. Lupan, O. Lupan, F. Schütt, R. Adelung and N. Stock, *ACS Appl. Mater. Interfaces*, 2023, **15**, 38674–38681.
15 X. Wu, S. Xiong, Z. Mao, S. Hu and X. Long, *Chem.–Eur. J.*, 2017, **23**, 7969.
16 H. Kim, W. Kim, S. Cho, J. Park and G. Y. Jung, *ACS Appl. Mater. Interfaces*, 2020, **12**, 28616–28623.
17 G. Lu, B. Zong, T. Tao, Y. Yang, Q. Li and S. Mao, *ACS Sens.*, 2024, **9**, 1916–1926.
18 B. Zong, Q. Xu and S. Mao, *ACS Sens.*, 2022, **7**, 1874–1882.
19 Q. Xu, B. Zong, Q. Li, X. Fang, S. Mao and K. Ostrikov, *J. Hazard. Mater.*, 2022, **424**, 127492.
20 W. P. Lustig, S. Mukherjee, N. D. Rudd, A. V. Desai, J. Li and S. K. Ghosh, *Chem. Soc. Rev.*, 2017, **46**, 3242–3285.
21 D. Sheberla, L. Sun, M. A. B. Forsythe, S. Er, C. R. Wade, C. K. Brozek, A. A. Guzik and M. Dincă, *J. Am. Chem. Soc.*, 2014, **136**, 8859–8862.
22 C. Huang, X. Shang, X. Zhou, Z. Zhang, X. Huang, Y. Lu, M. Wang, M. Löffler, Z. Liao, H. Qi, U. Kaiser, D. Schwarz, A. Fery, T. Wang, S. C. B. Mannsfeld, G. Hu, X. Feng and R. Dong, *Nat. Commun.*, 2023, **14**, 3850.
23 H. Yuan, G. Liu, Z. Qiao, N. Li, P. J. S. Buenconsejo, S. Xi, A. Karmakar, M. Li, H. Cai, S. J. Pennycook and D. Zhao, *Adv. Mater.*, 2021, **33**, 2101257.
24 K. Ikigaki, K. Okada, Y. Tokudome, T. Toyao, P. Falcaro, C. J. Doonan and M. Takahashi, *Angew. Chem., Int. Ed.*, 2019, **58**, 6886–6890.
25 B. Liu, M. Ma, D. Zacher, A. Bétard, K. Yusenko, N. M. Nolte, C. Wöll and R. A. Fischer, *J. Am. Chem. Soc.*, 2011, **133**, 1734–1737.
26 M. S. Yao, J. W. Xiu, Q. Q. Huang, W. H. Li, W. W. Wu, A. Q. Wu, L. A. Cao, W. H. Deng, G. E Wang and G. Xu, *Angew. Chem., Int. Ed.*, 2019, **58**, 14915–14919.
27 H. Yuan, N. Li, W. Fan, H. Cai and D. Zhao, *Adv. Sci.*, 2022, **9**, 2104374.
28 J. Wu, J. Chen, C. Wang, Y. Zhou, K. Ba, H. Xu, W. Z. Bao, X. Xu, A. Carlsson, S. Lazar, A. Meingast, Z. Sun and H. Deng, *Adv. Sci.*, 2020, **7**, 1903003.
29 D. Sabaghi, Z. Wang, P. Bhauriyal, Q. Lu, A. Morag, D. Mikhailovia, P. Hashemi, D. Li, C. Neumann, Z. Liao, A. M. Dominic, A. S. Nia, R. Dong, E. Zschech, A. Turchanin, T. Heine, M. Yu and X. Feng, *Nat. Commun.*, 2023, **14**, 760.
30 K. Liu, J. Réhault, B. Liang, M. Hambsch, Y. Zhang, S. Seçkin, Y. Zhou, R. Shivhare, P. Zhang, M. Polozij, T. A. F. König, H. Qi, S. Zhou, A. Fery, S. C. B. Mannsfeld, U. Kaiser, T. Heine, N. Banerji, R. Dong and X. Feng, *Adv. Mater.*, 2023, **35**, 2303288.
31 A. Bag and N. E. Lee, *J. Mater. Chem. C*, 2019, **7**, 13367–13383.
32 M. Shafiei, F. Hoshyargar, J. L. Duffin, C. Piloto, N. Motta and A. P. O' Mullane, *J. Phys. Chem. C*, 2015, **119**, 22208–22216.
33 M. K. Smith, K. E. Jensen, P. A. Pivak and K. A. Mirica, *Chem. Mater.*, 2016, **28**, 5264–5268.
34 M. G. Campbell, D. Sheberla, S. F. Liu, T. M. Swager and M. Dincă, *Angew. Chem., Int. Ed.*, 2015, **127**, 4423–4426.
35 M. Ko, A. Aykanat, M. K. Smith and K. A. Mirica, *Sensors*, 2017, **17**, 2192.
36 Z. Meng, A. Aykanat and K. A. Mirica, *J. Am. Chem. Soc.*, 2018, **141**, 2046–2053.
37 M. S. Yao, J. J. Zheng, A. Q. Wu, G. Xu, S. S. Nagarkar, G. Zhang, M. Tsujimoto, S. Sakaki, S. Horike and K. Otake, *Angew. Chem., Int. Ed.*, 2020, **59**, 172–176.
38 D. Kim, D. W. Kim, W. G. Hong and A. Coskun, *J. Mater. Chem. A*, 2016, **4**, 7710–7717.
39 J. E. Ellis, Z. Zeng, S. I. Hwang, S. Li, T. Y. Luo, S. C. Burkert, D. L. White, N. L. Rosi, J. J. Gassensmith and A. Star, *Chem. Sci.*, 2019, **10**, 737–742.
40 Y. Pu, W. Wu, J. Liu, T. Liu, F. Ding, J. Zhang and Z. Tang, *RSC Adv.*, 2018, **8**, 18604–18612.
41 A. Mohmeyer, A. Schaate, B. Hoppe, H. A. Schulze, T. Heinemeyer and P. Behrens, *Chem. Commun.*, 2019, **55**, 3367–3370.
42 H. Jiang, X. C. Liu, Y. Wu, Y. Shu, X. Gong, F. S. Ke and H. Deng, *Angew. Chem., Int. Ed.*, 2018, **57**, 3916–3921.
43 B. Bueken, N. V. Velthoven, T. Willhammar, T. Stassin, I. Stassen, D. A. Keen, G. V. Baron, J. F. M. Denayer, R. Ameloot, S. Bals, D. D. Vos and T. D. Bennett, *Chem. Sci.*, 2017, **8**, 3939–3948.
44 J. Hou, A. F. Sapnik and T. D. Bennett, *Chem. Sci.*, 2020, **11**, 310–323.
45 O. Shekhah, J. Liu, R. A. Fischer and C. Wöll, *Chem. Soc. Rev.*, 2011, **40**, 1081–1106.
46 I. Stassen, N. Burtch, A. Talin, P. Falcaro, M. Allendorf and R. Ameloot, *Chem. Soc. Rev.*, 2017, **46**, 3185–3241.
47 O. Yassine, O. Shekhah, A. H. Assen, Y. Belmabkhout, K. N. Salama and M. Eddaoudi, *Angew. Chem., Int. Ed.*, 2016, **55**, 15879–15883.
48 M. S. Yao, W. X. Tang, G. E. Wang, B. Nath and G. Xu, *Adv. Mater.*, 2016, **28**, 5229–5324.
49 N. A. Travlou, K. Singh, E. R. Castellón and T. J. Bandosz, *J. Mater. Chem. A*, 2015, **3**, 11417–11429.
50 H. J. Lin, J. P. Baltrus, H. Gao, Y. Ding, C. Y. Nam, P. Ohodnicki and P. X. Gao, *ACS Appl. Mater. Interfaces*, 2016, **8**, 8880–8887.
51 M. Z. Dai, Y. L. Lin, H. C. Lin, H. W. Zan, K. T. Chang, H. F. Meng, J. W. Liao, M. J. Tsai and H. Cheng, *Anal. Chem.*, 2013, **85**, 3110–3117.
52 M. S. Yao, X. J. Lv, Z. H. Fu, W. H. Li, W. H. Deng, G. D. Wu and G. Xu, *Angew. Chem., Int. Ed.*, 2017, **56**, 16510–16514.
53 H. Yuan, N. Li, J. Linghu, J. Dong, Y. Wang, A. Karmakar, J. Yuan, M. Li, P. J. S. Buenconsejo, G. Liu, H. Cai, S. J. Pennycook, N. Singh and D. Zhao, *ACS Sens.*, 2020, **5**, 1474–1481.
54 N. A. Travlou, K. Singh, E. R. Castellón and T. J. Bandosz, *J. Mater. Chem. A*, 2015, **3**, 11417–11429.
55 M. G. Campbell, S. F. Liu, T. M. Swager and M. Dincă, *J. Am. Chem. Soc.*, 2015, **137**, 13780–13783.
56 P. Wang, X. Zou, H. Tan, S. Wu, L. Jiang and G. Zhu, *J. Mater. Chem. C*, 2018, **6**, 5412–5419.
57 K. Xu, N. Li, D. Zeng, S. Tian, S. Zhang, D. Hu and C. Xie, *ACS Appl. Mater. Interfaces*, 2015, **7**, 11359–11368.

 

58 S. J. Kim, H. J. Koh, C. E. Ren, O. Kwon, K. Maleski, S. Y. Cho, B. Anasori, C. K. Kim, Y. K. Choi, J. Kim, Y. Gogotsi and H. T. Jung, *ACS Nano*, 2018, **12**, 986–993.
59 B. Zhao, J. Zhang, W. Feng, Y. Yao and Z. Yang, *Phys. Rev. B: Condens. Matter Mater. Phys.*, 2014, **90**, 201403.
60 B. Vishwanadh, T. S. R. C. Murthy, A. Arya, R. Tewari and G. K. Dey, *J. Alloys Compd.*, 2016, **671**, 424–434.
61 J. Qiao, X. Kong, Z. Hu, F. Yang and W. Ji, *Nat. Commun.*, 2014, **5**, 4475.
62 A. M. Eagleton, M. Ko, R. M. Stolz, N. Vereshchuk, Z. Meng, L. Mendecki, A. M. Levenson, C. Huang, K. C. MacVeagh, A. M. Shakib, J. J. Mahle, G. W. Peterson, B. G. Frederick and K. A. Mirica, *J. Am. Chem. Soc.*, 2022, **144**, 23297–23312.